PAPER • OPEN ACCESS

General framework for nonclassical nucleation

New Journal of Physics
The open access journal at the forefront of physics

Deutsche Physikalische Gesellschaft DPG
IOP Institute of Physics

Published in partnership with: Deutsche Physikalische Gesellschaft and the Institute of Physics

OPEN ACCESS

RECEIVED
4 January 2018

REVISED
25 June 2018

ACCEPTED FOR PUBLICATION
5 July 2018

PUBLISHED
17 August 2018

PAPER

General framework for nonclassical nucleation

Miguel A Durán-Olivencia[1,3], Peter Yatsyshin[1], Serafim Kalliadasis[1] and James F Lutsko[2]

[1] Complex Multiscale Systems Group, Department of Chemical Engineering, Imperial College London, London SW7 2AZ, United Kingdom
[2] Center for Nonlinear Phenomena and Complex Systems, Code Postal 231, Université Libre de Bruxelles, Blvd. du Triomphe, B-1050 Brussels, Belgium
[3] Author to whom any correspondence should be addressed.

E-mail: m.duran-olivencia@imperial.ac.uk **and** s.kalliadasis@imperial.ac.uk

Keywords: nonlcassical nucleation, phase transitions, fluctuating hydrodynamics, nucleation precursors

Abstract

A great deal of experimental evidence suggests that a wide spectrum of phase transitions occur in a multistage manner via the appearance and subsequent transformation of intermediate metastable states. Such multistage mechanisms cannot be explained within the realm of the classical nucleation framework. Hence, there is a strong need to develop new theoretical tools to explain the occurrence and nature of these ubiquitous intermediate phases. Here we outline a unified and self-consistent theoretical framework to describe both classical and nonclassical nucleation. Our framework provides a detailed explanation of the whole multistage nucleation pathway showing in particular that the pathway involves a single energy barrier and it passes through a dense phase, starting from a low-density initial phase, before reaching the final stable state. Moreover, we demonstrate that the kinetics of matter inside subcritical clusters favors the formation of nucleation clusters with an intermediate density, i.e. nucleation precursors. Remarkably, these nucleation precursors are not associated with a local minimum of the thermodynamic potential, as commonly assumed in previous phenomenological approaches. On the contrary, we find that they emerge due to the competition between thermodynamics and kinetics of cluster formation. Thus, the mechanism uncovered for the formation of intermediate phases can be used to explain recently reported experimental findings in crystallization: up to now such phases were assumed a consequence of some complex energy landscape with multiple energy minima. Using fundamental concepts from kinetics and thermodynamics, we provide a satisfactory explanation for the so-called nonclassical nucleation pathways observed in experiments.

1. Introduction

Phase transitions from less dense states to more dense ones are omnipresent in a wide spectrum of natural phenomena around us [1, 2]. Examples can be found in cloud and polar cap formation [3–5], biomineralization processes such as bone development [6–8], protein aggregation and colloidal crystallization in living cells [9–11], and volcano and black hole formation [12, 13]. These transitions are characterized by an initial incubatory stage governed by random density fluctuations that appear spontaneously in the mother phase (*nucleation clusters*). The incubatory stage determines the transition time and is known as *nucleation*.

One of the most popular approaches to nucleation is the so-called classical nucleation theory (CNT) [1, 2]. It relies on the Gibbsian concept of an energy barrier resulting from the competition between the volume and surface energies of the nucleation cluster [14, 15], and one empirically postulates monomer attachment-detachment rates, which are then used to describe the kinetics of cluster formation [16–21]. Moreover, nucleation clusters are assumed to be spherical seeds of the final phase, which grow in size by attaching monomers, as the transition ensues.

Over the years, CNT has been useful in explaining near-equilibrium transitions in simple fluids. However, recent experimental evidence has revealed new phenomena that seem to be irreconcilable with its basic ideas

[22–39], ranging from *multistage nucleation pathways* [22, 30, 32, 36, 37, 39], to *nucleation precursors* [23, 29, 31, 33, 34, 39] and *pre-nucleation clusters* [24, 27]. These experimental findings and associated phenomena are widely referred to as *nonclassical nucleation*. It is ubiquitous in a large spectrum of phase transitions, but progress to its understanding is hampered by the lack of a theoretical framework going beyond CNT. Of course CNT has been quite successful at equilibrium or close to it, but its use far from equilibrium is problematic relying on ad hoc and phenomenological hypotheses. For example, driven by the convenience and simplicity of CNT, there have been attempts to identify precursors and intermediate states in experiments by postulating an energy landscape with multiple local minima (metastable states) between the initial and the final stable state. However, unlike what is suggested by such postulated energy landscapes with multiple minima, it has been recently shown that nonclassical multistage nucleation does not necessarily mean multiple nucleation events [40–42]. This underlines the need for caution when trying to understand nonclassical nucleation through CNT-tinted glasses, and naturally raises the following question. Is it possible to come up with a solid theoretical justification for the nonclassical features of nucleation? To address this question we must change our viewpoint of nucleation clusters. Instead of treating them as discrete and independent objects, we need to think of them as spontaneous local density variations of the mother phase. In this case, the cluster evolution is given by the conservation laws of fluid dynamics augmented to account for spontaneous thermal fluctuations [43]. Within this framework, commonly known as fluctuating hydrodynamics (FH), the system is described by its time-dependent hydrodynamic fields. In the prototypical case of an isothermal system with strong dissipation due to the thermal bath, the only relevant quantity is the density field [44]. In principle, the equations of FH provide us with a full and self-contained description of the system's dynamics, including rare events, such as nucleation. Therefore, describing the evolution of a single density fluctuation using FH would provide an alternative theory of nucleation. A decisive first step in this direction was the recent mesoscopic nucleation theory (MeNT) put forward in [45–48]. In MeNT the number of parameters (so-called order parameters) we may choose to effectively describe a nucleation cluster is free.

As numerous experimental findings on nonclassical nucleation cannot be satisfactorily explained by one-parameter clusters, the development of new models by considering multi-parameter clusters may seem to be an appealing (if not *the only*) way to advance our understanding of nucleation. It would seem that finer effects associated with nucleation may ultimately be explained by ascribing additional degrees of freedom to nucleation clusters, e.g. the crystallinity, which measures local order inside the cluster. However, the rising complexity of such multi-parameter models means that exact expressions for observables, such as nucleation rate and cluster distribution, do not necessarily exist, even for the vanilla two-parameter model accounting for changes in the size and inner density of the cluster (the first necessary step towards a nonCNT). Under the MeNT picture, such observable quantities are approximated by utilizing the concepts of mean first-passage time (MFPT) and the equilibrium distribution derived from the corresponding Fokker–Planck equation, respectively [45–48]. Nevertheless, beyond the simplest one-parameter model, these approximations also rise in complexity, which might be an important factor that has hindered the applicability of MeNT so far. The fundamental question then is whether or not it is possible to formulate a fundamental and flexible theory of nucleation capable of capturing nonclassical aspects, but with the simplicity and ease of access of the classical picture.

This is precisely the aim of the present study. Using elements from differential geometry and stochastic calculus we show that *any* multi-parameter model can be reduced to an analytically tractable one-parameter model by following the nucleation pathway, i.e. the most-likely path (MLP) of the system. Since, in principle, the nucleation pathway of a given system may be obtained from simulations or even direct measurements, e.g. atomic force microscopy [49], our results provide a valuable practical tool to explain and quantify nucleation experiments. The theoretical effort to reduce the FH picture to a general one-parameter description is worthwhile as it leads to the derivation of simple analytic expressions for the nucleation rate and cluster distribution function, given the nucleation pathway. These expressions should be accessible to nucleation practitioners as they allow the estimation of quantities such as nucleation rate and cluster distribution without the need for the equilibrium approximation. And should provide practitioners with a self-contained and self-consistent theoretical framework, which can potentially explain and quantify *any* nonclassical aspects of nucleation. To showcase the predictive power of the methodology developed in this work, we apply it to the two-parameter model mentioned before (accounting for changes in the size and inner density of the cluster), to reduce it to a general one-parameter description, and demonstrate that the cluster distribution function obtained corroborates the existence of intermediate nucleation states, which can be linked to the highly debated nucleation precursors [23, 29, 31, 33, 34, 37, 39, 50]. Surprisingly, we observe that these nucleation precursors are not associated with energy minima in the traditional sense, but are rather temporarily stabilized by the small-scale kinetics of matter inside the nucleation cluster. More importantly, our work provides a formal and alternative answer to the question of the role played by kinetics in nucleation, and whether the observation of nucleation precursors should be understood as a unique consequence of a complex energy landscape. Finally, it is worth mentioning that the formal framework presented here is not limited to the study of nucleation

precursors, which is only one of many possible features of nonclassical nucleation. Applied to more general models for nucleation clusters (including new order parameters, e.g. crystallinity), it will provide estimations of the observable quantities mentioned above, i.e. the nucleation rate and cluster distribution.

2. Formulation

Our starting point is the FH description of nonequilibrium systems (which in turn can be obtained from the full microscopic description i.e. Hamilton's equations, figure A1), with an additional assumption of the FH dynamics being overdamped. Nucleation is then fully described by the evolution of the one-body density $\rho(\mathbf{r}, t)$ of the system, which is reasonable for most cases of practical interest. We note that in the thermodynamic description of uniform equilibrium systems, $\rho(\mathbf{r}, t) = \rho$ is equivalent to the average number density. The overdamped limit of the system dynamics essentially means that the evolution is driven by the thermodynamic force $\nabla\delta F[\rho]/\delta\rho(\mathbf{r}, t)$, where $F[\rho]$ is an appropriate generalized thermodynamic potential, such as the free-energy, which allows us to define the energy barrier $\Omega[\rho] = F[\rho] - \mu N$ in the grand canonical ensemble [51]. Here μ and N are the chemical potential and the total number of particles, respectively. The equilibrium states are computed by minimization of Ω which is the state-of-the-art in classical density functional theory (e.g. [52, 53]). Within the FH approach, the nucleation clusters are associated with the spatially localized fluctuations of density that are brought about by thermal noise.

To connect the theory with experimental observations, the density fluctuation (nucleation cluster) must be described in terms of measurable properties, such as cluster radius, inner density, crystallinity, etc. Formally, this is achieved by introducing a parameterization in terms of these properties:

$$\rho(\mathbf{r}; t) = \rho(r; x^1(t), \ldots, x^N(t)), \tag{1}$$

where $\mathbf{x} = (x^1, \ldots, x^N)$ are the order parameters shaping the energy barrier $\Omega[\rho] = \Omega(\mathbf{x})$. The cluster cumulative mass $m(r; \mathbf{x}(t))$, given by

$$m(r; \mathbf{x}(t)) = \int_{r'<r} \mathrm{d}\mathbf{r}'\rho(\mathbf{r}'; \mathbf{x}(t)), \tag{2}$$

is then inserted into the FH equation, yielding the N stochastic differential equations which describe the noisy dynamics of the order parameters (see figure A1). The statistics across various realizations of noise is summarized by the MLP, which represents the nucleation pathway. The key now is to obtain the nucleation path, $\Gamma = (\tilde{x}^1(s), \ldots, \tilde{x}^N(s))$ representing a trajectory in the parameter space, where s is the natural (arc-length) parameter of such a curve. The critical cluster is hence characterized by the values of the order parameters fulfilling:

$$\left(\frac{\partial\beta\Omega(\mathbf{x}(s))}{\partial\mathbf{x}(s)}\right)_{\mathbf{x}_c} = \left(\frac{\partial\beta\Omega(s)}{\partial s}\right)_{s_c=\Gamma^{-1}(\mathbf{x}_c)} = 0, \tag{3}$$

with $\beta = 1/k_BT$ being the inverse thermal energy at a given temperature T.

2.1. Natural dynamics

In many practical situations, the nucleation pathway may be accessible from, e.g., simulations, microscopic mean-field theories or even experiments measuring the evolution of the nucleation clusters. As there is very little chance that experimental observation will capture unlikely pathways, the nucleation trajectory observed must lie in the close vicinity of the MLP (figure 1). In this case, the N order parameters will follow the nucleation pathway trajectory in the average sense, and can be expressed in terms of the arc-length s. The latter, thus, becomes the only relevant order parameter for nucleation, which locates the cluster properties along the nucleation pathway. The arc-length dynamics is governed by the equation (see appendix A):

$$\frac{\mathrm{d}s}{\mathrm{d}t} = -Dg^{-1}(s)\frac{\partial\beta\Omega(s)}{\partial s} - \frac{D}{2}g^{-2}(s)\frac{\partial g(s)}{\partial s} + \sqrt{Dg^{-1}(s)}\,\xi(t), \tag{4}$$

with D the diffusion constant and $g^{-1}(s)$ the kinetic (or Onsager) coefficient of the evolution of the order parameter s, given by

$$g(s) = \int_0^\infty \mathrm{d}r\,\frac{1}{4\pi r^2\rho(r; s)}\left(\frac{\mathrm{d}m(r; s)}{\mathrm{d}s}\right)^2, \tag{5}$$

which recovers the usual expression for the monomer attachment rate for diffusion-limited nucleation (e.g. equation (10.18) of [1]) in the simplest case of one-parameter model for clusters [46].

Thus, the first term on the right-hand side of equation (4) represents the effective drift that clusters experience along the nucleation pathway, i.e. along the s-axis (see figure 1), with $-\partial\beta\Omega(s)/\partial s$ playing the role of the thermodynamic driving force. The last term depends on the fluctuating force $\xi(t)$, which has zero mean and

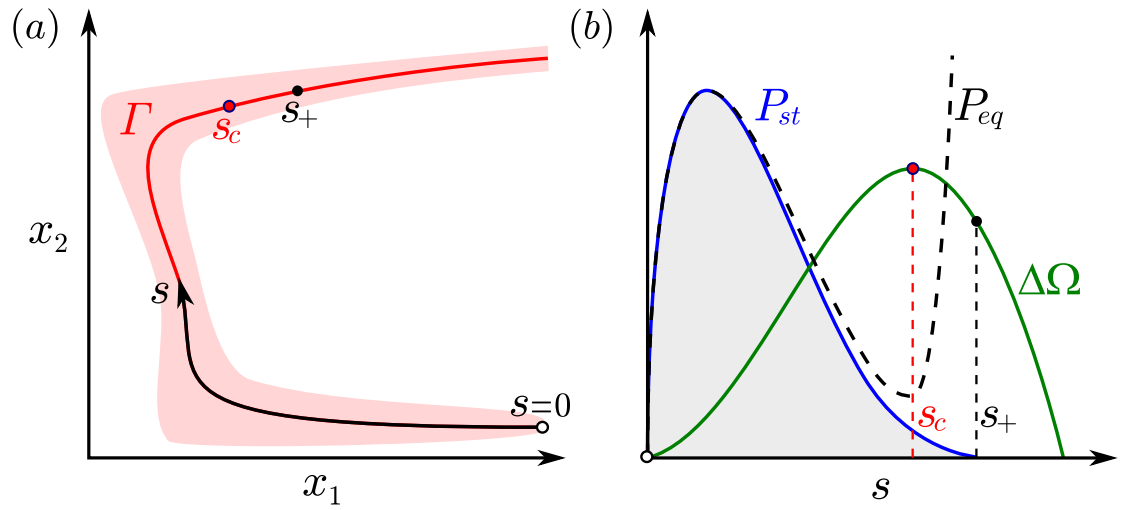

Figure 1. Sketch of nonclassical nucleation. The initial cluster is denoted by an open circle. (a) Nucleation pathway $\Gamma(s)$, parameterized by its arc-length s, corresponds to the MLP followed by two order parameters, $x_1(s)$ and $x_2(s)$. An initial density fluctuation at $s = 0$ evolves along $\Gamma(s)$ in the average sense. The shading around the pathway represents the fact that a particular realization of nucleation may deviate from the MLP. Red circle at $s = s_c$ denotes the critical cluster. Black circle at $s = s_+$ demarcates the boundary between nucleation and growth regimes. (b) Energy barrier $\Delta\Omega(s)$ (green curve) and cluster distribution $P_{st}(s)$ (blue curve) along the nucleation pathway. The dashed black curve represents a simplified treatment, which uses the cluster distribution in an undersaturated solution.

is delta-correlated in time. The second term has its origin in the noise, arising from the Itô–Stratonovich inequivalence [46]. Due to its origin, it is also known as the spurious drift and vanishes in the weak-noise limit (WNL), i.e. while the effective drift dominates the dynamics.

2.2. Nucleation cluster distributions

The stochastic dynamics along the nucleation pathway given by equation (4) yields a time-dependent cluster distribution, which measures the probability of observing a nucleation cluster with properties around a given s, at a given time t. Due to the rare-event nature of nucleation, the cluster distribution relaxes (almost) instantaneously to a steady-state distribution $P_{st}(s)$. During the nucleation stage, the probability of finding a cluster out of the metastable basin must be close to zero. Hence, we assume that P_{st} vanishes at a certain point beyond the critical cluster, $s_+ > s_c$. This point demarcates the boundary of the nucleation regime, so that beyond such configuration s_+ the nucleation cluster will deterministically grow without a bound. Therefore, the probability of observing a nucleation cluster around position s on the MLP is given by (see appendix B)

$$P_{st}(s) = A\sqrt{g(s)}\ \mathrm{e}^{-\beta\Omega(s)} \int_s^{s_+} \mathrm{d}s'\ \sqrt{g(s')}\ \mathrm{e}^{\beta\Omega(s')}, \tag{6}$$

where A is the normalization constant and $s_+ = (1 + \epsilon)s_c$ the (empirical) boundary between the nucleation and growth stages on the MLP, where $0 < \epsilon \ll 1$. For an undersaturated equilibrium solution, there is only one energy minimum, and no barrier crossing, so the distribution takes the simple form

$$P_{eq}(s) = A \exp\left\{-\beta\Omega(s) + \frac{1}{2}\log(g(s))\right\}. \tag{7}$$

To make analytical progress, and obtain estimates of observable quantities such as the nucleation rate, CNT uses a kind of detailed-balance relation to get the monomer-detachment rate from the monomer attachment frequency by utilizing the equilibrium distribution [1], even though this can really only be true at equilibrium. Equation (6), however, provides an exact nonequilibrium cluster distribution for supersaturated solutions independently of the number of order parameters. This is precisely why equation (6) is central to the present study. For low and moderate supersaturated solutions[4], the flux of nucleating clusters is almost negligible, which makes nucleation a rare-event. Understanding the exponent in equation (7) as an effective energy barrier, $\beta\Omega_{\mathrm{eff}}(s)$, the cluster distribution recovers the classical Gibbs–Boltzmann structure, assumed heuristically in phenomenological descriptions. However, Ω_{eff} is not an equilibrium thermodynamic potential but a generalization that incorporates the small-scale kinetics of cluster formation, unlike CNT or other heuristic approaches. Such an abstraction allows us to explore the likelihood of appearance of nucleation clusters with given properties via the analysis of the effective energy barrier (see figure 1).

[4] We refer to high supersaturation when the energy barrier involved gives $\mathrm{e}^{-\beta\Delta\Omega_c} > \mathcal{O}(10^{-2})$. For moderate supersaturation, $\mathcal{O}(10^{-5}) < \mathrm{e}^{-\beta\Omega_c} < \mathcal{O}(10^{-3})$. Finally, low supersaturation is used when $\mathrm{e}^{-\beta\Omega_c} < \mathcal{O}(10^{-6})$.

2.3. Nucleation rate and time

We can use the formalism outlined so far to obtain an exact expression for the main quantity of interest in nucleation experiments, the nucleation rate J. This quantity measures the mean production rate of super-critical clusters (i.e., $s > s_c$), which in turn determines the mean time required for the nucleation cluster to abandon the metastable basin (i.e., $0 \leqslant s < s_c$). The nucleation rate is commonly characterized by the MFPT, the inverse of which is assumed proportional to the nucleation rate. However, in general, there is no exact expression for the MFPT for more than one-parameter, but an approximation only valid in the WNL [47, 54–56]. The main advantage of the most-likely approach adopted here is that the nucleation process is entirely described in terms of only one-parameter, the arc-length. Generalizing the derivation of the nucleation rate for one-parameter MeNT [46], we obtain the expression for the *most-likely nucleation rate* of an N-parameter model (see appendix C):

$$J[\Gamma] = \frac{\rho_\infty}{2\, t_n[\Gamma]}, \tag{8}$$

$$t_n[\Gamma] = \int_0^{s_c} \mathrm{d}s N(s) \frac{\sqrt{g(s)}}{2D} \mathrm{e}^{-\beta\Omega(s)} \int_s^{s_+} \mathrm{d}s' \sqrt{g(s')}\, \mathrm{e}^{\beta\Omega(s')}, \tag{9}$$

with ρ_∞ the average number density of the metastable mother phase (i.e., at an infinite distance from the center of the nucleation cluster) and $N(s)$ the total number of molecules in the cluster. Equation (9) naturally defines the most-likely time for nucleation to occur. Hence, we refer to t_n as the *nucleation time*. The square brackets have been added to remind us that the corresponding quantities depend on the curve describing the nucleation pathway.

3. Results

The simplest model of cluster that captures the essence of nonclassical nucleation is determined by two basic properties of nucleation clusters: the radius and the density at the center. Essentially, a nucleation cluster is divided into three parts: the surrounding mother phase with density ρ_∞, the inner core with density ρ_0 and radius R, and the depletion zone which enforces mass conservation. This translates into a two-dimensional parameterization of the cluster density, $\rho(r; \mathbf{x}(t)) = \rho(r; \rho_0, R)$. In order to compute the energy of cluster formation, $\Delta\Omega = \Omega(\rho_0, R) - \Omega(\rho_\infty, \infty)$, one requires a reliable approximation for the bulk fluid equation of state (EOS). We use the Barker–Henderson perturbation theory with the reference system given by the Carnahan–Starling EOS for the hard-sphere fluid [57, 58] and the perturbative part given by the ten Wolde–Frenkel model (see appendix D), which is well-suited for the description of globular proteins [40]. The EOS allows us to obtain the equilibrium bulk densities at coexistence for a given temperature (e.g [53, 58]), $\rho_\infty^{(c)}$ (vapor-like) and $\rho_0^{(c)}$ (liquid-like). These values define the coexistence (saturation) curve of the fluid. The mean-field expression for the grand free-energy allows us to obtain the surface tension of the planar interface, $\gamma^{(c)}$, as an increment of the grand potential at coexistence. With this, we can eventually compute the work of cluster formation (with $T = 0.4$, in reduced units), shown in figure 2. In the WNL, the nucleation pathway (i.e., the MLP) can be computed by setting the cluster at the critical configuration $\mathbf{x}_c = (\rho_c, R_c)$ (i.e., the saddle point of the energy barrier), perturbing slightly along the unstable direction and integrating the deterministic parts of the governing equations for R and ρ_0 (see figure A1). This yields the curve Γ, red solid line in figure 2 [47]. As can be observed, the MLP does not follow the Cartesian gradient of the free-energy, i.e. $\mathbf{e}_i \partial_i \Omega$ with $\mathbf{e}_i$ being the local unit vector pointing in the coordinate direction $i \in \{\rho_0, R\}$. This is because, in general coordinates, i.e. $\mathbf{x}$, the gradient is defined in terms of the metric tensor g^{ij}, which in turn defines the length in the $\mathbf{x}$-space [45, 47] (see also appendix A). Indeed, the gradient operator can be written as $\mathbf{e}_i g^{ij} \partial_j$ (with $g^{ij} = g_{ij}^{-1}$ being the components of the inverse of the tensor g_{ij}) using Einstein's summation convention. The components of the metric tensor g_{ij} are defined in equation (A.7), which in the particular case of a two-parameter model translates into equations (D.11)–(D.13). The free-energy barrier is discussed in appendix D. We note that $\rho_0(\Gamma)$ and s, are connected by a one-to-one relationship, as shown in figure 3. This means that the nucleation pathway can be equivalently parameterized either by the arc-length or by the more physically meaningful order parameter, ρ_0. For this reason, we prefer to use ρ_0, since it provides a more physical information about the properties of the nucleation cluster.

3.1. Energy barrier

Having determined the nucleation pathway, we can apply the theoretical framework discussed in section 2. A first, and essential, result that emerges from it is the most-likely energy barrier, i.e. $\beta\Delta\Omega[\Gamma]$. According to the previous discussion, the energetic cost of producing a nucleation cluster is computed as a function of ρ_0, figures 4 and 5. For the two-parameter model, the energy barrier along the nucleation pathway reveals a highly

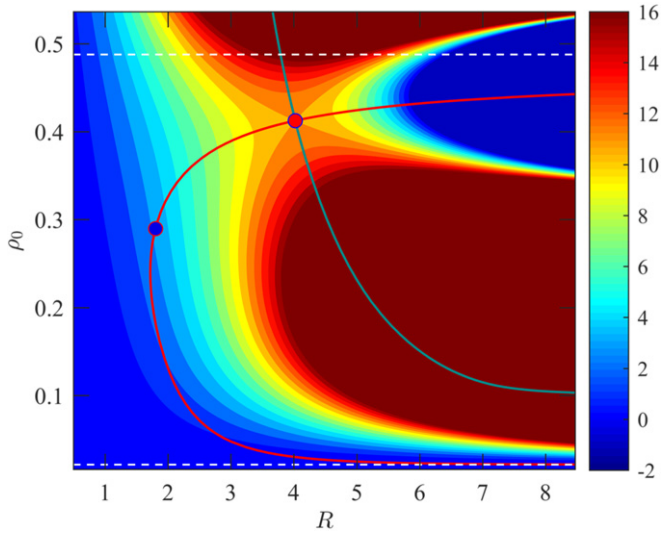

Figure 2. Work of cluster formation $\beta\Delta\Omega(\rho_0, R)$ at $k_B T = 0.4\epsilon_0$, with $\rho_\infty = 1.4\ \rho_\infty^{(c)}$. White dashed lines indicate the initial metastable state density ρ_∞ (bottom) and the final stable-liquid density (top), $\rho_0^\ell \sim 1.04\ \rho_0^{(c)}$. The origin of the ρ_0-axis is set at the coexistence vapor density $\rho_\infty^{(c)} \sim 1.5 \times 10^{-2}\sigma^{-3}$. The two minima of $\beta\Omega$ occur at densities ρ_∞ and ρ_0^ℓ. The red and green solid lines represent the MLP, i.e. Γ, and the separatrix between the two basins of attraction, respectively. The red filled circle represents the critical nucleation cluster, i.e. the saddle point of the energy surface, with $\rho_c = 0.84\rho_0^{(c)}$ and $R_c = 1.01\ R_c^{\mathrm{CNT}}$ where $R_c^{\mathrm{CNT}} = 3.98\sigma$. The blue filled circle shows the precursor state predicted by the constrained two-parameter model (see figure 8).

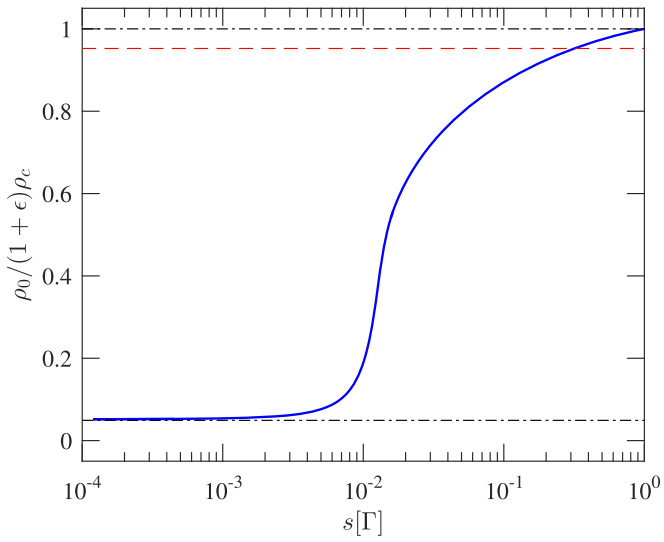

Figure 3. One-to-one correspondence between the cluster central density, ρ_0, and the arc-length, s, over the MLP. The uppermost horizontal line corresponds to the value of the post-critical density, $\rho_0^+ = (1 + \epsilon)\rho_c$ (with $\epsilon = 10^{-1}$). The red dashed line shows the density of the critical cluster, equation (3). The lowermost horizontal line is the density of the initial metastable state, in this case $\rho_\infty = 1.4\ \rho_\infty^{(c)}$.

nonclassical form. In figure 5(a), the horizontal axis seems to be naturally divided into three intervals according to the energy and thermodynamic driving force involved. This determines the different kind of clusters present in a nucleation process. First, the work of cluster formation varies rapidly as ρ_0 grows up to a certain value, after which a plateau is reached. These low-density values represent small deviations from the background density with associated large radii (see figure 2), and feel a relatively strong thermodynamic driving force (given by the slope), leading to their disappearance. Between those low-density clusters and the near-critical clusters, with densities in the vicinity of the maximum of $\beta\Delta\Omega$, we find a broad range of cluster densities with very similar energies. Besides involving a low energetic cost, the clusters with these intermediate densities experience an almost negligible thermodynamic driving force, which indicates that these 'intermediate' clusters are very likely to appear and remain for long time periods within the initial metastable solution. Intuitively, we can expect these intermediate clusters to be identified as nucleation precursors. This is indeed the case as we will confirm in the

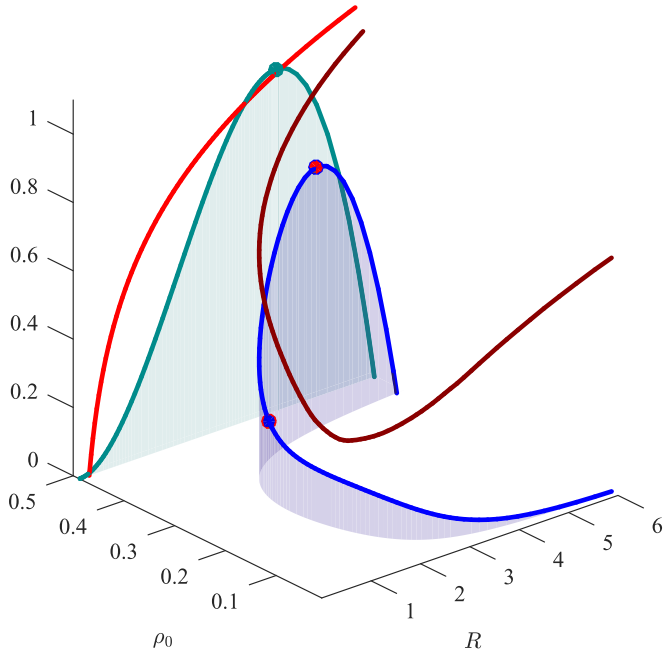

Figure 4. Normalized work of cluster formation, $\Delta\Omega/\Delta\Omega_{\mathrm{CNT}}(s_c)$, and normalized kinetic contribution, $\log(g(s))/\log(g(s_+))$, along the nucleation pathway. Green and blue lines represent the energy barriers predicted by CNT and the two-parameter model, respectively, along their respective nucleation pathways. These are expanded independently along their respective natural order parameter in figure 5. Brown and red curves are the kinetic contributions predicted by our framework and CNT, respectively. Such contributions are included in the effective energy barrier, shown in figure 6.

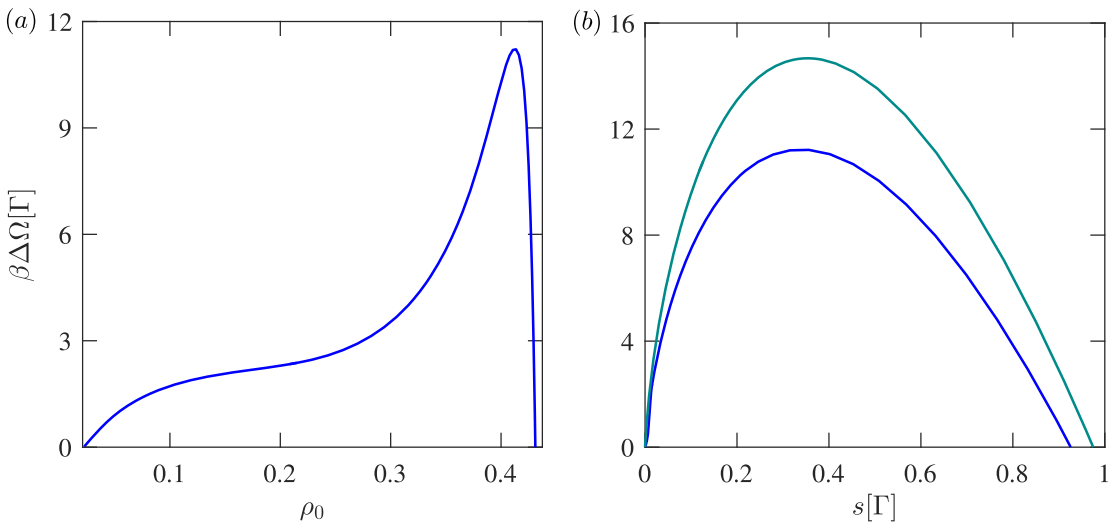

Figure 5. (a) Work of cluster formation along the nucleation pathway Γ. The blue line was computed by using equation (D.9) along Γ. (b) Work of cluster formation as function of the natural parameter s. The green line represents the CNT estimation along the classical nucleation pathway. The global maxima correspond to the critical cluster, with properties R_c and ρ_c given in figure 2.

following section, with the computation of the effective energy barrier and the nucleation cluster distribution. Finally, beyond the critical density we find the post-critical clusters, subjected to a high thermodynamic driving force pushing them to grow without a bound. While the results shown in figures 4 and 5 correspond to a moderate supersaturation, with $\rho_\infty = 1.4\ \rho_\infty^{(c)}$, the same behavior is found for any supersaturation values.

Figures 4 and 5 depict a direct comparison between our predictions and CNT. We note that in the CNT framework the nucleation pathway is just a straight line with $\rho_0 = \rho_0^{(c)}$ and R varying from $R = 0$ up to $R = R_+ = (1 + \epsilon)R_c$ (not shown in figure 4). Both predictions appear qualitatively similar when represented as a function of the natural parameter, s, figure 5(b), in the sense that they both exhibit a local maximum corresponding to the height of the nucleation barrier (which determines the nucleation critical cluster). But there is a substantial difference between the two maxima of approximately 5 k_BT. Such a discrepancy is related to

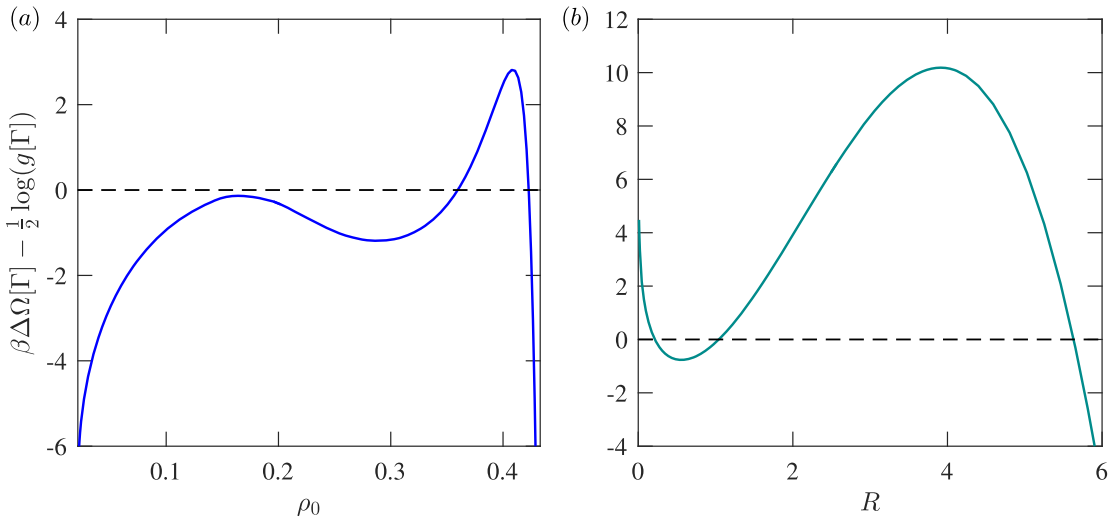

Figure 6. Effective energy barrier along the nucleation pathway Γ. The color code is the same as in figure 5. (a) Two minima within $\rho_0 < \rho_c$. The first, lower energetic one, corresponds to long-wavelength fluctuations. The second, intermediate one, represents an intermediate density state purely induced by kinetics. This local minimum has an associated radius, $R_m = 0.45R_c$. (b) Effective energy of cluster formation within the CNT framework.

the fact that in CNT $\rho_0 = \rho_0^{(c)}$, whereas the two-parameter model allows the inner density to freely vary. This has a considerable effect on nucleation rate estimations, given the functional dependence of J on the energy barrier, equation (8).

3.2. Probability distribution: the effective energy barrier

One of the most important results is the existence of an exact nonequilibrium expression for the nucleation cluster distribution, equation (6). This quantity is crucial when it comes to understanding the cluster population and its properties, bypassing the standard but controversial equilibrium approximation. In fact, equation (6) allows us to test the reliability of this approximation in equation (7) which was not possible before (it is expected to be valid close to equilibrium, i.e. low supersaturation as noted earlier).

As discussed in section 2, the effective energy barrier shapes the nucleation cluster distribution in most practical cases. It is shown in figures 6 and 7, comparing the prediction from CNT [46] with that from the two-parameter model equation (7). Within the CNT framework, figure 6(b), the kinetic term $\frac{1}{2}\log g(s)$ induces a local minimum far from the critical cluster, R_c. This minimum corresponds to a maximum of likelihood. In the near vicinity of the local minimum predicted by CNT, clusters also show a negative effective energy, whereas out of this basin their energy approaches rapidly values higher than k_BT. From a purely thermodynamic point of view, one would argue that clusters become more unstable (and, hence, unlikely) as the radius grows, because the free-energy cost involved grows monotonically as R, up to R_c. However, the kinetics of the process shifts the energy barrier in a way that stabilizes very small clusters (monomers), making them very likely despite involving a nonzero work of formation.

The more realistic two-parameter model reveals a completely different picture to the one depicted by CNT, figure 6(a). First, only near-critical clusters have a positive effective energy, meaning that almost all precritical clusters with $\rho_\infty \leqslant \rho_0 < \rho_c$ have a non-negligible probability. The outcome is a much richer cluster distribution that spreads all over the precritical states, not governed by monomers only, as is the case in CNT. This can be seen as the result of the fact that the theory allows clusters to access a broader region of the phase space than CNT does, which has only an isolated minimum. Second, the kinetic term does not affect all the intermediate clusters the same way and induces a local minimum at an intermediate density ρ_m, such that $\rho_\infty < \rho_m < \rho_c$. The competition between thermodynamics and kinetics causes an intermediate state with a substantial probability about ρ_m, thus behaving as nucleation precursors. We recall that the local intermediate minimum, identified as an intermediate precursor state, does not come from a minimum of the thermodynamic free-energy, Ω, but as a result of including the mass-transport kinetics inside the nucleation cluster. This demonstrates that apparent multi-step energy barriers can be the result of the kinetics of cluster formation, while actually involving just a single energy barrier.

The above analysis is corroborated by computing the steady-state PDF, figure 8. The usefulness of the effective energy barrier now becomes clear, as the equilibrium PDF (dashed line) only differs from the steady-state PDF (solid line) for post-critical clusters. Hence, one can infer the actual cluster distribution and its

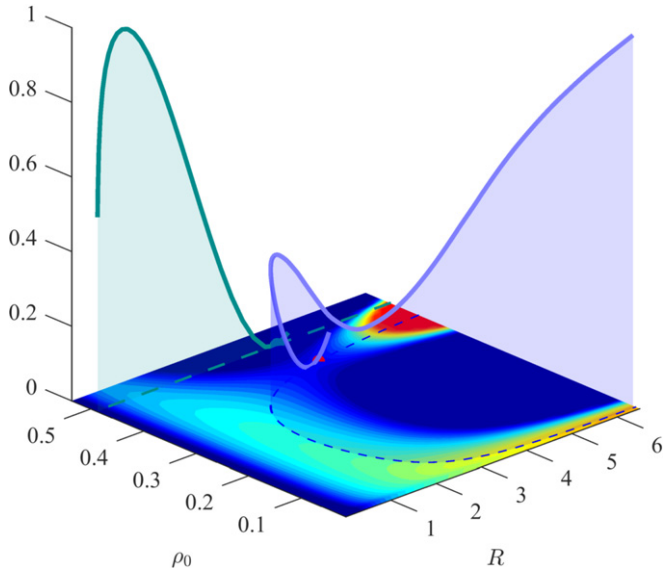

Figure 7. Representation of the equilibrium cluster distribution, equation (7), along the classical (green curve) and nonclassical (blue curve) pathways. For graphical convenience, the distributions are normalized to their maximum amplitudes. Such distributions are independently represented as a function of the corresponding order parameter in figure 8. Surface plot at the bottom shows the effective potential $\beta\Delta\Omega(\mathbf{x}) - \log\sqrt{\det g(\mathbf{x})}$, with $\mathbf{x} = (\rho_0, R)$.

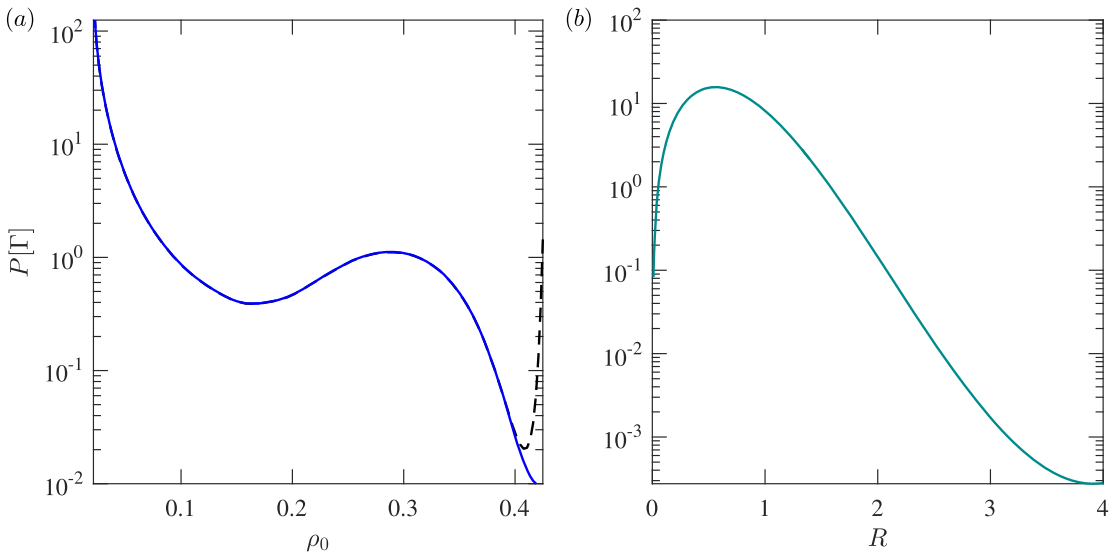

Figure 8. Nucleation cluster distribution along the nonclassical (a) and classical (b) pathways. Solid lines represent the exact steady-state solution, equation (6). Black dashed line goes for the equilibrium approximation, equation (7). Nonclassical cluster distribution (a) shows a maximum at an intermediate density (nucleation precursor), in perfect agreement with the minimum reported for the effective energy barrier in figure 6. Proof that several maxima in the cluster distribution do not necessarily imply several minima in the thermodynamic potential.

properties as previously discussed. It is also evident that the main effect of the integral term in equation (6) is to guarantee the boundary condition at $\rho_0 = \rho_+$. Again, the CNT prediction was computed and shown, figure 8(b), together with the results from the formalism introduced in section 2 to highlight the differences between both theories.

3.3. Nucleation rates

We can now contrast the second most important quantity in nucleation, the nucleation times (or rates) predicted by the different models we have discussed so far, using equation (9) and the CNT estimate given in appendix D. The results (in reduced units) are shown in figure 9 as a function of both the supersaturation ratio $S = \rho_\infty/\rho_\infty^{(c)}$, and the nucleation barrier, $\beta\Omega_c$, respectively. It is noteworthy that the predictions obtained with

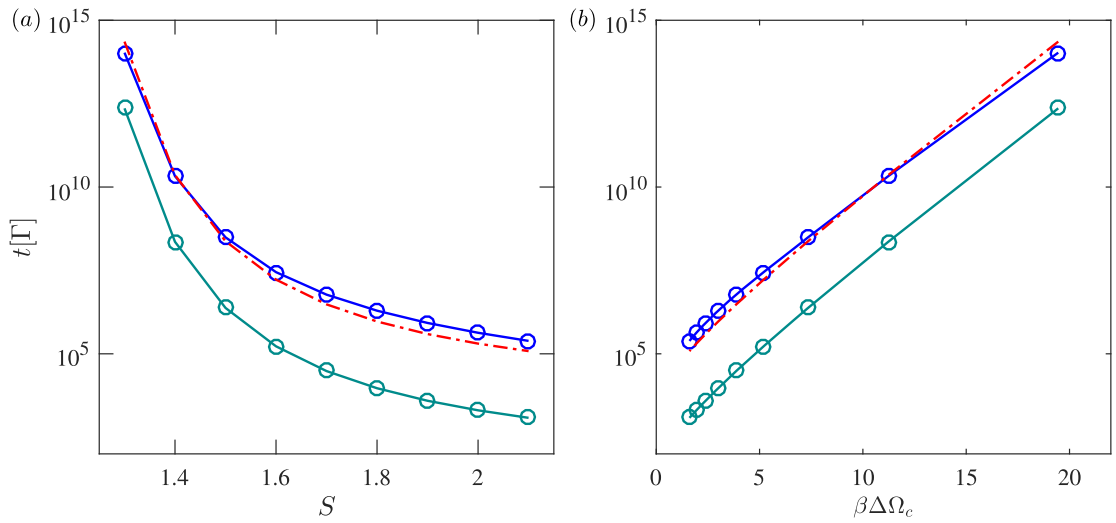

Figure 9. Nondimensional nucleation times predicted by our framework (blue line) and CNT (green line), equations (9) and (D.5), respectively. There is a systematic difference between CNT and our framework of approximately two orders of magnitude. This is shown by the red dashed line, which represents the CNT estimation multiplied by 10^2. (a) Nucleation time as a function of the supersaturation ratio S. (b) Nucleation time as a function of the nucleation barrier, $\beta\Delta\Omega_c = \beta\Delta\Omega(s_c)$.

equation (9) deviate from CNT by approximately two orders of magnitude in a systematic way (indeed, the deviations of CNT predictions from experimental nucleation rates have been noted and widely debated over the last few decades). This observation corroborates previous experimental works, e.g. [26, 38, 59–61], where dramatic differences between CNT and experiments have been observed. For instance, in the case of proteins, it has been shown experimentally that CNT tends to overestimate the nucleation rate by several orders of magnitude (e.g. [26]), in agreement with our findings. Further, in the case of water, it has been reported that CNT systematically overestimates nucleation rates with respect to experimental observations (in qualitative agreement with our results) by approximately two orders of magnitude [61]. It is this qualitative agreement that makes us believe that the framework outlined here offers a complete and rational understanding of nonclassical nucleation, and in a way that clarifies the elementary dynamic characteristics of nonclassical nucleation.

4. Conclusions

We have introduced a general theoretical framework to describe nonclassical nucleation with simple and exact analytical expressions. By taking the nucleation process to follow the most-likely route after the initial metastable state, we obtain exact expressions for both the nucleation cluster distribution and the nucleation rate and time. Our framework is capable of describing complex nonclassical features of nucleation but with equations of the same level of simplicity as CNT. Analyzing the cluster distribution, we observe that the stability of the nucleation clusters is governed by an effective energy barrier which includes the kinetics of matter inside the nucleation cluster. Such an effective barrier could, in principle, have an arbitrary number of intermediate local minima depending on the complexity of the kinetic coefficient but showing no intermediate states in the thermodynamic potential. This highlights the importance of the cluster kinetics in describing the ubiquitous multistage nucleation pathways and nucleation precursors, among other nonclassical features. Moreover, although the theory is tested here with only one- and two-parameter models of nucleation clusters, it is generic, hence not restricted to the specific conditions considered, and can be used in a wide spectrum of other settings, e.g. crystallization by including a third order parameter such as the crystallinity (along with a more sophisticated free-energy functional).

Applying our framework to a particular model of clusters characterized by the inner density and the size of the cluster, we obtain deviations from the CNT predictions for the nucleation rate similar to previous works. But we also go much further. In particular, unlike previous works we study the nonequilibrium distribution of clusters. This is done with the help of the effective energy barrier defined in section 2. Our main conclusion is that the predicted nucleation cluster distribution is much richer than the CNT prediction, due to the intrinsic kinetics of the process, which is naturally incorporated to the energy barrier in a self-consistent manner. Indeed, the system seems to follow the formation of intermediate density (precritical) clusters, i.e. nucleation precursors. Even more, the kinetics of cluster formation favors the appearance of clusters with density very close to that of the critical cluster. This mechanism of formation of nucleation precursors offers insights on the origin of

seemingly stable precritical clusters that have been recently observed in experiments. Indeed, we find that the appearance of nucleation precursors can be a direct result of a complex competition between kinetics and thermodynamics, without having to involve complicated energy landscapes as commonly postulated.

Finally, interesting applications of the framework developed here would be to consider multiple-particle species and confined geometries. These conditions seem to be the canonical experimental setting to observe nonclassical nucleation (such as the widely known pre-nucleation clusters or the two-step nucleation mechanism, which lack a formal theoretical explanation as of yet). Also, another interesting study would be the application of our framework to scrutinise the effects of inter-particle hydrodynamic interactions on nucleation. These interactions might have an impact on diffusivity, and hence, on particle dynamics, which has been shown to be crucial to understanding certain features of nonclassical nucleation. We shall examine these and related questions in future studies.

Acknowledgments

We are grateful to Alexander ES Van Driessche and Mike Sleutel for stimulating discussions and extensive comments on an early draft of this paper. We acknowledge financial support from the Engineering and Physical Sciences Research Council of the UK through Grants No. EP/L027186, EP/L020564, EP/L025159 and EP/K503733 (EPSRC-Imperial College Pathways to Impact-Impact Acceleration Award), from the European Research Council through Advanced Grant No. 247031 and from the European Space Agency under Contract No. ESA AO-2004-070.

Appendix A. Derivation of the arc-length dynamics

As mentioned at the beginning of section 2, our starting point is the overdamped FH equation for colloidal systems (figure A1) [44]:

$$\frac{\partial}{\partial t}\rho(\mathbf{r};\,t) = \nabla\cdot\left(D\rho(\mathbf{r};\,t)\nabla\frac{\delta\beta F[\rho]}{\delta\rho(\mathbf{r})}\right) + \nabla\cdot\sqrt{D\rho(\mathbf{r};\,t)}\;\boldsymbol{\xi}(\mathbf{r};\,t) \tag{A.1}$$

with $\boldsymbol{\xi}(\mathbf{r};\,t)$ being a zero mean and delta-correlated fluctuating force, such that $\langle\boldsymbol{\xi}(\mathbf{r};\,t)\rangle = 0$ and $\langle\boldsymbol{\xi}(\mathbf{r};\,t)\boldsymbol{\xi}(\mathbf{r}';\,t')\rangle = 2\delta(t-t')\delta(\mathbf{r}-\mathbf{r}')$. Integrating equation (A.1) over a spherical shell gives an evolution equation for the cumulative mass $m(r;\,t)$ of spherically symmetric density distributions $\rho(r;\,t)$ [45]:

$$\frac{\partial m(r;\,t)}{\partial t} = D4\pi r^2\rho(r;\,t)\frac{\partial}{\partial r}\frac{\delta\beta F[\rho]}{\delta\rho(\mathbf{r})} + \sqrt{D4\pi r^2\rho(r;\,t)}\;\xi(r;\,t), \tag{A.2}$$

with $m(r;\,t)$ defined as in equation (2), $\xi(r;\,t)$ having zero mean and $\langle\xi(r;\,t)\xi(r';\,t')\rangle = 2\delta(r-r')\delta(t-t')$. Consider now the parameterization of the density profile of a fluctuation in terms of a collection of scalar parameters $\mathbf{x} = (x_1, \ldots, x_N)$, so that $\rho(\mathbf{r};\,t) = \rho(r;\,\mathbf{x}(t))$. Hence, $m(r;\,t) = m(r;\,\mathbf{x}(t))$, so that:

$$\frac{\partial m(r;\,\mathbf{x}(t))}{\partial x_i}\frac{\mathrm{d}x_i}{\mathrm{d}t} = D4\pi r^2\rho(r;\,t)\frac{\partial}{\partial r}\frac{\delta\beta F[\rho]}{\delta\rho(\mathbf{r})}\bigg|_{\rho(r;\mathbf{x}(t))} + \sqrt{D4\pi r^2\rho(r;\,t)}\;\xi(r;\,t). \tag{A.3}$$

The latter equation can be multiplied by a test function $W_j(r;\,\mathbf{x}(t))$ and integrated over r, resulting into:

$$\begin{aligned} g_{ij}(\mathbf{x}(t))\frac{\mathrm{d}x_i}{\mathrm{d}t} = {} & D\int_0^\infty \mathrm{d}r\; W_j(r;\,\mathbf{x}(t))4\pi r^2\rho(r;\,t)\frac{\partial}{\partial r}\frac{\delta\beta F[\rho]}{\delta\rho(\mathbf{r})}\bigg|_{\rho(r;\mathbf{x}(t))} \\ & + \int_0^\infty \mathrm{d}r\; W_j(r;\,\mathbf{r}(t))\sqrt{D4\pi r^2\rho(r;\,t)}\;\xi(r;\,t), \end{aligned} \tag{A.4}$$

with

$$g_{ij}(\mathbf{x}(t)) = \int_0^\infty \mathrm{d}r\; W_j(r;\,\mathbf{x}(t))\frac{\partial m(r;\,\mathbf{x}(t)}{\partial x_i}. \tag{A.5}$$

Equation (A.2) can be given the geometric interpretation of a gradient flow on the energy surface in mass space with a metric of $(\partial m(r;\,t)/\partial r)^{-1}$. This allows us to define the distance between two mass distributions as [45]:

$$s[m_0,\,m_1] = \sqrt{\int_0^\infty \mathrm{d}u(m_0^{-1}(u) - m_1^{-1}(u))^2}. \tag{A.6}$$

It can be shown that the definition of g_{ij} which minimizes the distance between the parameterized mass distribution $m(r;\,\mathbf{x}(t))$ and the actual mass distribution $m(r;\,t)$ is the one involving the following definition for $W_j(r;\,\mathbf{x}(t))$:

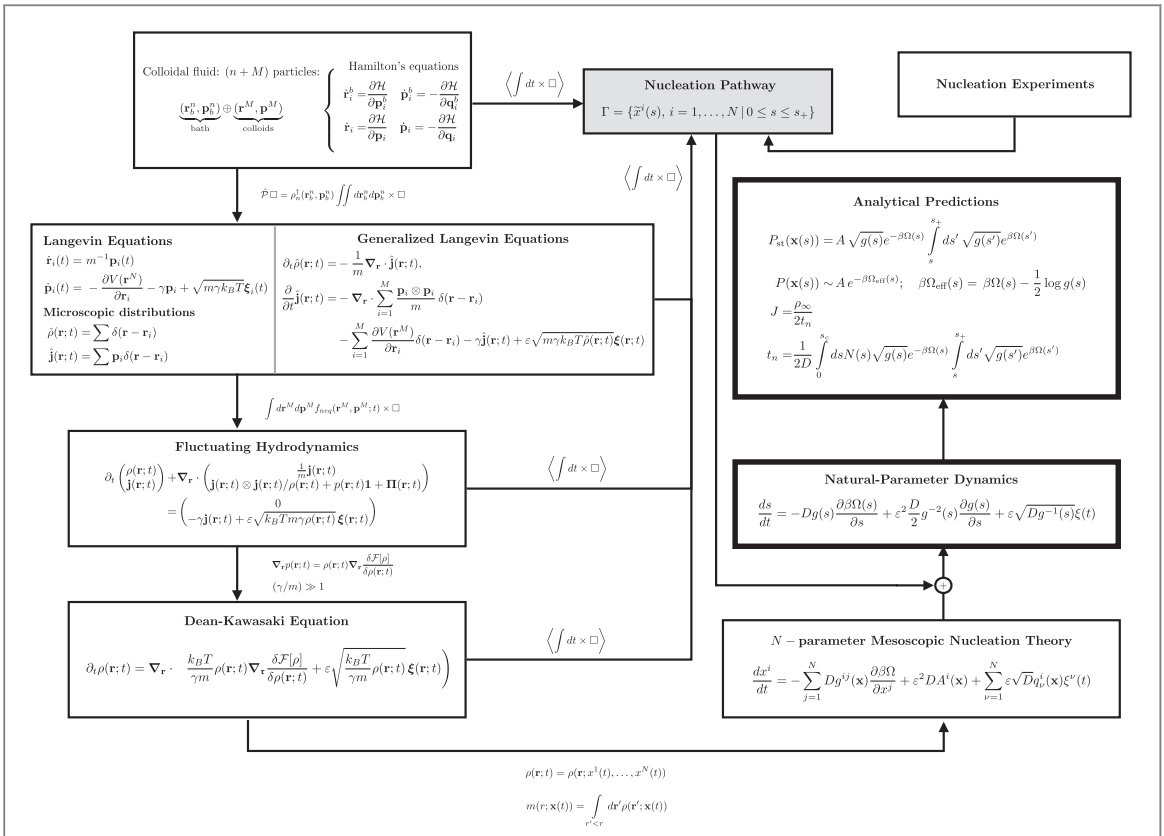

Figure A1. Flow diagram of the approach used to obtain the expressions presented in this work from the full underlying particle dynamics. Arrows indicate the interconnectedness of the different equations. Thick boxes: main results of this work. Text on arrows give brief descriptions of the approximations/manipulations made. Nomenclature: $\hat{\mathcal{P}}$ projection operator, f_{neq} nonequilibrium distribution, $\gamma/m \gg 1$ overdamped limit, and $\langle \int \mathrm{d}t \times \square \rangle$ time integration and average over multiple realizations [44].

$$W_j(r;\,\mathbf{x}(t)) = \frac{1}{4\pi r^2 \rho(r;\,\mathbf{x}(t))}\frac{\partial m(r;\,\mathbf{x}(t))}{\partial x_j},$$
$$g_{ij}(\mathbf{x}(t)) = \int_0^\infty \mathrm{d}r\, \frac{1}{4\pi r^2 \rho(r;\,\mathbf{x}(t))}\frac{\partial m(r;\,\mathbf{x}(t))}{\partial x_i}\frac{\partial m(r;\,\mathbf{x}(t))}{\partial x_j}. \tag{A.7}$$

We can carry out the integration on the first term on the right-hand side of equation (A.4), which produces

$$\begin{aligned}\int_0^\infty \mathrm{d}r\; W_j(r;\,\mathbf{x}(t))4\pi r^2\rho(r;\,t)\frac{\partial}{\partial r}\frac{\delta\beta F[\rho]}{\delta\rho(\mathbf{r})}\bigg|_{\rho(r;\mathbf{x}(t))} &= \int_0^\infty \mathrm{d}r\; \frac{\partial m(r;\,\mathbf{x}(t))}{\partial x_j}\frac{\partial}{\partial r}\frac{\delta\beta F[\rho]}{\delta\rho(\mathbf{r})}\bigg|_{\rho(r;\mathbf{x}(t))}\\ = \lim_{r\to\infty}\left(\frac{\partial m(r;\,\mathbf{x}(t))}{\partial x_j}\frac{\delta\beta F[\rho]}{\delta\rho(\mathbf{r})}\bigg|_{\rho(r;\mathbf{x}(t))}\right) - \int_0^\infty \frac{\partial\rho(r;\,\mathbf{x}(t))}{\partial x_j}\frac{\delta\beta F[\rho]}{\delta\rho(\mathbf{r})}\bigg|_{\rho(r;\mathbf{x}(t))}\mathrm{d}\mathbf{r}\\ = \frac{\partial N(\mathbf{x}(t))}{\partial x_j}\beta\mu - \frac{\partial\beta F(\mathbf{x})}{\partial x_j},\end{aligned} \tag{A.8}$$

where we have used that $\lim_{r\to\infty} m(r;\,\mathbf{x}(t)) = N(\mathbf{x}(t))$, the total number of particles in the system, and that the system is expected to have bulk properties at infinity, so that $\lim_{r\to\infty}(\delta F[\rho]/\delta\rho(\mathbf{r}))_{\rho(r;\mathbf{x}(t))} = \mu$. The second term in equation (A.8) was obtained by using the functional chain rule, so that $F(\mathbf{x}) = F[\rho(\mathbf{x})]$. Upon substitution of equations (A.8) into (A.4) we obtain:

$$\frac{\mathrm{d}x_i}{\mathrm{d}t} = -Dg_{ij}^{-1}\frac{\partial\beta\Omega(\mathbf{x})}{\partial x_j} - g_{ij}^{-1}(\mathbf{x})\int_0^\infty \mathrm{d}r\,\sqrt{\frac{D}{4\pi r^2\rho(r;\,\mathbf{x})}}\frac{\partial m(r;\,\mathbf{x})}{\partial x_j}\xi(r;\,t), \tag{A.9}$$

where we have also made use of the definition of the (Landau's) grand potential $\Omega = F - \mu N$. Equation (A.9) must be interpreted in the Stratonovich sense, since the equation is not Itô–Stratonovich equivalent and we have used the usual chain rule for derivatives. In order to get a simpler form for the noise term, we first need to obtain the Itô representation of equation (A.9) and then substitute the noise term with a simpler one with the same autocorrelation. Utilizing the standard Itô–Stratonovich transformation rule [62], we get the equivalent Itô form:

$$\frac{\mathrm{d}x_i}{\mathrm{d}t} = -Dg_{ij}^{-1}\frac{\partial\beta\Omega(\mathbf{x})}{\partial x_j} + \int_0^\infty \mathrm{d}r\left(\frac{\partial}{\partial x_l}g_{ij}^{-1}(\mathbf{x})\sqrt{\frac{D}{4\pi r^2\rho(r;\,\mathbf{x})}}\frac{\partial m(r;\,\mathbf{x})}{\partial x_j}\right)\left(g_{lk}^{-1}(\mathbf{x})\sqrt{\frac{D}{4\pi r^2\rho(r;\,\mathbf{x})}}\frac{\partial m(r;\,\mathbf{x})}{\partial x_k}\right) - g_{ij}^{-1}(\mathbf{x})\int_0^\infty \mathrm{d}r\,\sqrt{\frac{D}{4\pi r^2\rho(r;\,\mathbf{x})}}\frac{\partial m(r;\,\mathbf{x})}{\partial x_j}\xi(r;\,t), \tag{A.10}$$

where Einstein's summation convention was used for simplicity. The noise term in equation (A.10) has autocorrelation D_{ij} given as follows:

$$D_{ij}(\mathbf{x}) = g_{ik}^{-1}g_{jl}^{-1}\int_0^\infty \mathrm{d}r\,\frac{2D}{4\pi r^2\rho(r;\,\mathbf{x})}\frac{\partial m(r;\,\mathbf{x})}{\partial x_k}\frac{\partial m(r;\,\mathbf{x})}{\partial x_l} = 2Dg_{ij}^{-1}(\mathbf{x}). \tag{A.11}$$

Thus, the noise term can be replaced by the simpler form $\sqrt{D}\,q_{ij}^{-1}(\mathbf{x})\xi_j(t)$ with $g_{ij}(\mathbf{x}) = q_{ik}(\mathbf{x})q_{jk}(\mathbf{x})$ and $\langle\xi_i(t)\xi_j(t)\rangle = 2\delta_{ij}\delta(t-t')$. The second term in the right-hand side of equation (A.10) is the noise-induced (so-called spurious) drift, with components $h_i^{(I)}(\mathbf{x})$, under Itô's interpretation. For Itô–Stratonovich equivalent equations, this term vanishes. After some manipulations, this term can be rewritten as follows:

$$D^{-1}h_i^{(I)}(\mathbf{x}) = \frac{\partial g_{ij}^{-1}(\mathbf{x})}{\partial x_j} + \frac{1}{2}g_{ij}^{-1}g_{lk}^{-1}\frac{\partial g_{lk}(\mathbf{x})}{\partial x_j} + \frac{1}{2}(g_{ij}^{-1}(\mathbf{x})g_{lk}^{-1}(\mathbf{x}) - g_{lj}^{-1}(\mathbf{x})g_{ik}^{-1}(\mathbf{x})) \times \int_0^\infty \mathrm{d}r\,\frac{1}{4\pi r^2\rho^2(r;\,\mathbf{x})}\frac{\partial\rho(r;\,\mathbf{x})}{\partial x_j}\frac{\partial m(r;\,\mathbf{x})}{\partial x_l}\frac{\partial m(r;\,\mathbf{x})}{\partial x_k}. \tag{A.12}$$

Thus, we arrive at the simplified version of equation (A.9) under Itô's interpretation:

$$\frac{\mathrm{d}x_i}{\mathrm{d}t} = -Dg_{ij}^{-1}(\mathbf{x})\frac{\partial\beta\Omega(\mathbf{x})}{\partial x_j} + h_i^{(I)}(\mathbf{x}) + \sqrt{D}\,q_{ij}^{-1}(\mathbf{x})\xi_j(t), \tag{A.13}$$

which is again a gradient flow on the energy surface in $\mathbf{x}$-space with g_{ij}^{-1} as metric. If we wanted to work under Stratonovich calculus, we could use the same equation but with the following noise-induced drift:

$$h_i^{(S)} = h_i^{(I)} - Dq_{kj}^{-1}\frac{\partial q_{ij}^{-1}}{\partial x_k}. \tag{A.14}$$

As mentioned before, the nucleation pathway is identified by the MLP, which is determined by the temporal evolution of the order parameters $\mathbf{x}(\tau)$. This can be seen as a parameterized curve, $\Gamma = \{(\tilde{x}_1(\tau), \ldots, \tilde{x}_N(\tau)):\, \tau\in[\tau_0,\,\tau_{\mathrm{end}}]\}$, where τ_0 and τ_{end} are the values of τ related to the initial and final state, respectively. That said, we can find a natural reparametrization of the curve by using the arc-length over the curve:

$$s(\tau) = \int_{\tau_0}^{\tau}\mathrm{d}\tau'\sqrt{\frac{\mathrm{d}x_i(\tau')}{\mathrm{d}\tau'}g_{ij}(\mathbf{x}(\tau'))\frac{\mathrm{d}x_j(\tau')}{\mathrm{d}\tau'}}, \tag{A.15}$$

so that, $\widetilde{\Gamma}(s) = \Gamma(\tau(s))$, where $\tau(s)$ is the inverse of $s(\tau)$. Under these conditions, the density profile can be re-parameterized as

$$\rho(r;\,t) \to \rho_\Gamma(r;\,s) = \rho(r;\,s,\,\mathbf{x}_\Gamma(s)) \tag{A.16}$$

which leads us to a single order parameter description of the dynamics. Applying the previous derivation to the case of a single parameter, equation (A.13) is simplified substantially as $g_{ij}(\mathbf{x})$ becomes $g(s)$, $q_{ij}(\mathbf{x})$ becomes $\sqrt{g(s)}$, and the noise-induced drift is simply $-\frac{1}{2}Dg^{-2}(s)\partial g(s)/\partial s$. Combining these results gives the desired equation for s:

$$\frac{\mathrm{d}s}{\mathrm{d}t} = -Dg^{-1}(s)\frac{\partial\beta\Omega(s)}{\partial s} - \frac{D}{2}g^{-2}(s)\frac{\partial g(s)}{\partial s} + \sqrt{Dg^{-1}(s)}\;\xi(t). \tag{A.17}$$

Besides, the definition of $g(s)$ given in equation (5), is readily obtained by using equation (A.7) with a single parameter s:

$$
\begin{aligned}
g(s) &= \int_0^\infty \mathrm{d}r\ \frac{1}{4\pi r^2 \rho(r;\, s)}\left(\frac{\partial m(r;\, s)}{\partial s}\right)^2 \\
&= \int_0^\infty \mathrm{d}r\ \frac{1}{4\pi r^2 \rho(r;\, s,\, \mathbf{x}_\Gamma)}\left(\frac{\partial m(r;\, s,\, \mathbf{x}_\Gamma)}{\partial s}\right)^2 \\
&\quad + \int_0^\infty \mathrm{d}r\ \frac{1}{2\pi r^2 \rho(r;\, s,\, \mathbf{x}_\Gamma)}\frac{\partial m(r;\, s,\, \mathbf{x}_\Gamma)}{\partial s}\frac{\partial m(r;\, s,\, \mathbf{x}_\Gamma)}{\partial x^j}\frac{\mathrm{d}x^j}{\mathrm{d}s} \\
&\quad + \int_0^\infty \mathrm{d}r\ \frac{1}{4\pi r^2 \rho(r;\, s,\, \mathbf{x}_\Gamma)}\frac{\partial m(r;\, s,\, \mathbf{x}_\Gamma)}{\partial x^j}\frac{\partial m(r;\, s,\, \mathbf{x}_\Gamma)}{\partial x^k}\frac{\mathrm{d}x^j}{\mathrm{d}s}\frac{\mathrm{d}x^k}{\mathrm{d}s}
\end{aligned}
\tag{A.18}
$$

where $\dot{\mathbf{x}}_\Gamma(s) = \left(\frac{\mathrm{d}x_1}{\mathrm{d}s}, \ldots, \frac{\mathrm{d}x_N}{\mathrm{d}s}\right)_\Gamma$.

Appendix B. Derivation of the most-likely cluster distribution

As shown in appendix A, the dynamics of the arc-length parameter s along the MLP is governed by the stochastic differential equation (4). Accordingly, the probability distribution $P(s;t)$ for observing a nucleation cluster at a certain position s on the MLP (see figure 1) at time t, satisfies the Fokker–Planck equation [62]:

$$
\frac{\partial P(s,\, t)}{\partial t} = -D\left(g^{-1}(s)\frac{\partial \beta\Omega(s)}{\partial s} + g^{-1/2}(s)\frac{\partial}{\partial s}g^{-1/2}(s)\right)P(s,\, t) \equiv -\frac{\partial \mathfrak{J}(s,\, t)}{\partial s} \tag{B.1}
$$

with $\mathfrak{J}(s)$ being the probability flux at s. While finding an exact analytical solution for equation (B.1) is a hard (if not impossible) problem, a simple case admitting a solution is that of a steady-state system with constant probability flux $\mathfrak{J}$. Under such conditions,

$$
\mathfrak{J} = -D\left(g^{-1}(s)\frac{\partial \beta\Omega(s)}{\partial s} + g^{-1/2}(s)\frac{\partial}{\partial s}g^{-1/2}(s)\right)P_{\mathrm{st}}(s), \tag{B.2}
$$

for which the steady-state distribution can be readily found:

$$
P_{\mathrm{st}}(s) = A\, g^{1/2}(s)\mathrm{e}^{-\beta\Omega(s)} - \frac{\mathfrak{J}}{D}g^{1/2}(s)\mathrm{e}^{-\beta\Omega(s)}\int^s g^{1/2}(z)\mathrm{e}^{\beta\Omega(z)}\mathrm{d}z, \tag{B.3}
$$

where A is a normalization constant. To ensure such a steady-state regime with nonzero flux, we have to impose a boundary condition that removes super-critical clusters once they reach a given size $s_+ > s_c$. Hence, imposing that the steady-state distribution must satisfy $P_{\mathrm{st}}(s_+) = 0$ results in the desired equation for the nucleation cluster distribution:

$$
P_{\mathrm{st}}(s) = \frac{\mathfrak{J}}{D}g^{1/2}(s)\mathrm{e}^{-\beta\Omega(s)}\int_s^{s_+} g^{1/2}(z)\mathrm{e}^{\beta\Omega(z)}\mathrm{d}z. \tag{B.4}
$$

Finally, the equilibrium regime is identified with a zero probability flux, i.e. $\mathfrak{J} = 0$. Therefore, when the system is an equilibrium (i.e. undersaturated) state, the cluster distribution will be given as follows,

$$
\begin{aligned}
P_{\mathrm{eq}}(s) &= A g^{1/2}(s)\exp(-\beta\Omega(s)) \\
&= A\exp\left(-\beta\Omega(s) + \frac{1}{2}\log g(s)\right).
\end{aligned}
\tag{B.5}
$$

Appendix C. Derivation of the most-likely nucleation rate

The nucleation rate measures the mean production rate of super-critical nuclei (i.e., $s > s_c$) per unit volume, which in turn determines the mean time required for the nucleation cluster to abandon the metastable basin (i.e., $0 \leqslant s < s_c$). Then

$$
J = \frac{1}{V}\frac{\mathrm{d}}{\mathrm{d}t}\int_{N_*}^\infty \mathrm{d}N\ N_c(t)P(N;\, t), \tag{C.1}
$$

where $N_* = N(s_c)$ is the number of molecules inside the critical nucleation cluster, $P(N;t)$ is the cluster distribution in terms of the number of molecules inside the cluster, $N_c(t) = \int_0^\infty \mathrm{d}N\ n(N;\, t)$ and $P(N;\, t) = \frac{n(N;t)}{\int_0^\infty \mathrm{d}N\ n(N;t)}$, so that $N_c(t)$ can be understood as the normalization constant of $P(N;t)$. Applying the time derivative in equation (C.1) and using equation (B.1):

$$J = \frac{1}{V}\frac{\mathrm{d}N_c(t)}{\mathrm{d}t}\int_{N_*}^{\infty}\mathrm{d}N\ P(N;\,t) + \frac{N_c(t)}{V}\int_{N_*}^{\infty}\mathrm{d}N\ \frac{\partial P(N;\,t)}{\partial t}$$
$$= \frac{1}{V}\frac{\mathrm{d}N_c(t)}{\mathrm{d}t}\int_{N_*}^{\infty}\mathrm{d}N\ P(N,\,t) + \frac{N_c(t)}{V}\mathfrak{J}(N_*;\,t). \tag{C.2}$$

For the steady-state with a constant probability flux, $\mathfrak{J}$, satisfying the boundary condition at s_+, the first term in equation (C.2) does not contribute, since $N_c(t) = N_c$, which eventually produces:

$$J = \frac{N_c}{V}\mathfrak{J}. \tag{C.3}$$

But P_{st} must be normalized, so that:

$$P_{\mathrm{st}}(s) = \frac{g^{1/2}(s)\mathrm{e}^{-\beta\Omega(s)}\int_s^{s_+} g^{1/2}(z)\mathrm{e}^{\beta\Omega(z)}\mathrm{d}z}{\int_0^{s_+}\mathrm{d}s\ g^{1/2}(s)\mathrm{e}^{-\beta\Omega(s)}\int_s^{s_+} g^{1/2}(z)\mathrm{e}^{\beta\Omega(z)}\mathrm{d}z} \tag{C.4}$$

which can be now substituted into equation (B.4) to eliminate $\mathfrak{J}$:

$$J = \frac{N_c}{V}\frac{D}{\int_0^{s_+}\mathrm{d}s\ g^{1/2}(s)\mathrm{e}^{-\beta\Omega(s)}\int_s^{s_+} g^{1/2}(z)\mathrm{e}^{\beta\Omega(z)}\mathrm{d}z}. \tag{C.5}$$

This still leaves the question of determining the total population of clusters N_c. To do that we can impose the following condition on the total number of molecules $\mathcal{N}(N_0)$ in clusters up to size N_0,

$$\mathcal{N}(N_0) = \int_0^{N_0}\mathrm{d}N\ Nn(N) = N_c\int_0^{N_0}\mathrm{d}N\ NP_{\mathrm{st}}(N) = N_c\int_0^{s(N_0)}\mathrm{d}s\ N(s)P_{\mathrm{st}}(s), \tag{C.6}$$

where we have made use of the covariant structure of the theory, so that $P(N)\mathrm{d}N = P(s)\mathrm{d}s$. Manipulating equation (C.6) yields:

$$N_c = \mathcal{N}(N_0)\frac{\int_0^{s_+}\mathrm{d}s\ g^{1/2}(s)\mathrm{e}^{-\beta\Omega(s)}\int_s^{s_+} g^{1/2}(z)\mathrm{e}^{\beta\Omega(z)}\mathrm{d}z}{\int_0^{s(N_0)}\mathrm{d}s\ N(s)g^{1/2}(s)\mathrm{e}^{-\beta\Omega(s)}\int_s^{s_+} g^{1/2}(z)\mathrm{e}^{\beta\Omega(z)}}. \tag{C.7}$$

After substitution of equations (C.7) into (C.5), we obtain the nucleation rate,

$$J(N_0) = \frac{D\ \overline{\rho}(N_0)}{\int_0^{s(N_0)}\mathrm{d}s\ N(s)g^{1/2}(s)\mathrm{e}^{-\beta\Omega(s)}\int_s^{s_+} g^{1/2}(z)\mathrm{e}^{\beta\Omega(z)}}, \tag{C.8}$$

where we have made use of the definition of the average density $\overline{\rho}(N_0) = \mathcal{N}(N_0)/V$. To remove the dependence on the parameter N_0, we will use $N_0 = N(s_c)$, so that $s(N_0) = s_c$. Finally, for low and moderate supersaturations we expect that most of the material exists in the form of small clusters, hence $\overline{\rho}(N_*) \sim \rho_\infty$. Combining these results we eventually obtain,

$$J = \frac{\rho_\infty}{2\ t_n},$$
$$t_n = \int_0^{s_c}\mathrm{d}sN(s)\frac{\sqrt{g(s)}}{2D}e^{-\beta\Omega(s)}\int_s^{s_+}\mathrm{d}s'\sqrt{g(s')}\,e^{\beta\Omega(s')} \tag{C.9}$$

where we have introduced the definition of the most-likely nucleation time, t_n.

Appendix D. Theoretical details

D.1. Interaction potential

The theoretical framework developed in this work was tested with a model globular protein, assumed to interact via the effective ten Wolde–Frenkel potential [40]:

$$v(r) = \begin{cases}\infty, & r < \sigma\\ \dfrac{4\epsilon_0}{\alpha^2}\left[\left(\dfrac{1}{\left(\frac{r}{\sigma}\right)^2 - 1}\right)^6 - \alpha\left(\dfrac{1}{\left(\frac{r}{\sigma}\right)^2 - 1}\right)^3\right], & r \geqslant \sigma,\end{cases} \tag{D.1}$$

where $\alpha = 50$, ϵ_0 is the depth of the potential well and σ is the hard-core radius. All numerical results in this work are reported in reduced units, using σ and ϵ_0 to scale lengths, energies and times.

D.2. CNT

Consider a system set initially in a metastable state with an average density ρ_∞, which will eventually nucleate a new phase of density $\rho_0^{(\mathrm{bulk})}$, such that

$$\omega^{(n)}(\rho_\infty) = \omega^{(n)}(\rho_0^{(\mathrm{bulk})}), \quad n = 0,\ 1, \tag{D.2}$$

with $\omega^{(n)}(\rho) = \frac{\mathrm{d}^n\omega(\rho)}{\mathrm{d}\rho^n}$ and $\omega(\rho) = f(\rho) - \mu\rho$, where $f(\rho)$ is the Helmholtz free-energy per unit volume and μ the chemical potential. The CNT framework is formulated on the basis that the nucleation clusters are governed by a single order parameter, the size of the aggregate. Thus, a model of the work of cluster formation is built assuming spherically symmetric clusters with the same density as the final stable state. Moreover, a sharp interface between the cluster and its surrounding is tacitly hypothesized. Thus:

$$\rho(r;\,\mathbf{x}) = \rho(r;\,R) = \rho_0\,\Theta(R - r) + \rho_\infty\Theta(r - R), \tag{D.3}$$

with $\rho_0 = \rho_0^{(\mathrm{bulk})}$ and $\Theta(r)$ being the Heaviside step function. As a result, the work of cluster formation is given by the widely known expression:

$$\Delta\Omega = \Omega(R) - \Omega_\infty = \frac{4\pi}{3}R^3\Delta\omega(\rho_0) + 4\pi R^2\gamma^{(c)}, \tag{D.4}$$

with $\gamma^{(c)}$ being the planar surface tension at coexistence and $\Delta\omega(\rho) = \omega(\rho) - \omega(\rho_\infty)$. From standard arguments [1, 20, 21, 63], the time-evolution equation for the nucleation cluster distribution, i.e. the corresponding Fokker–Planck equation, is readily obtained. From this and following classical arguments [1, 46], the CNT expression for the nucleation rate is derived:

$$J_{\mathrm{CNT}} = \frac{\frac{D}{4\pi}\left(\frac{\rho_\infty}{\rho_0 - \rho_\infty}\right)^2}{\int_{R_1}^{R_+}\mathrm{d}R\ R^3\exp(\beta\Delta\Omega(R))} = \frac{\rho_\infty}{t_{\mathrm{CNT}}} \tag{D.5}$$

with R_+ being any value bigger than the critical radius R_c. We note that the classical relationship between the nucleation rate and the escape time in equation (D.5) has been used to implicitly define t_{CNT}. This expression is not covariant, meaning that estimations made with it will depend on the choice of the order parameter [62]. However, the results produced by equation (D.5) and the covariant counterpart from one-parameter MeNT only differ slightly, as discussed in detail in previous works [46–48]. This way, we can use as a benchmark either t_{CNT} from equation (D.5) or the MFPT [47]:

$$t_{\mathrm{mfp}}^{\mathrm{CNT}} = \frac{\int_0^{R_c}\mathrm{d}R\ R^{3/2}\mathrm{e}^{\beta\Delta\Omega(R)}\int_0^{R}\mathrm{d}R'\ R'^{3/2}\mathrm{e}^{-\beta\Delta\Omega(R')}}{D\rho_\infty/4\pi(\rho_0 - \rho_\infty)^2} \tag{D.6}$$

interchangeably, for all practical purposes. The reason for the choice of equation (D.5) is that it is the standard CNT definition.

D.3. MeNT: two-parameter model expressions

The formal derivation of MeNT has been reviewed in appendix A and is sketched in figure A1. The two-parameter model of nucleation clusters was, for the first time, introduced in [47], and is given by:

$$\begin{aligned}\rho(r;\,R,\,\rho_0) = {}&\rho_0\,\Theta(R - r) + \rho_1\,\Theta(r - R)\Theta(R_1 - r)\\ &+ \rho_\infty\Theta(r - R_1)\end{aligned} \tag{D.7}$$

with ρ_1 being fixed by the conservation of the total mass, so that $R^3\rho_0 + (R_1^3 - R^3)\rho_1 = R_1^3\rho_\infty$. The radius R_1 fulfills:

$$R_1^3 = R_{\mathrm{max}}^3 + \lambda\left(\frac{\rho_0 - \rho_\infty}{\rho_\infty}\right)^2 R^3, \tag{D.8}$$

where R_{max} and λ are constants that must be provided to the model. A parametric study was carried out in [47], showing that R_{max} limits the size of clusters with density close to ρ_∞ and that λ modulates the accessible region of the parameter space. To avoid side effects, λ and R_{max} are set so that nearly all the parameter space is accessible. We take the values $\lambda = 10$ and $R_{\mathrm{max}} = 20\sigma$. The work of cluster formation related to this model, equations (D.7)–(D.8), is given by [47]:

$$\begin{aligned}\Delta\Omega(\rho_0,\,R) = {}&V(R)\Delta\omega(\rho_0) + \Delta\omega(\rho_1)(V(R_1) - V(R))\\ &+ K(\rho_1 - \rho_0)^2S(R) + K(\rho_\infty - \rho_1)^2S(R_1)\end{aligned} \tag{D.9}$$

with $V(r) = \frac{4\pi}{3}r^3$ and $K = \gamma^{(c)}/(\rho_0^{(c)} - \rho_\infty^{(c)})$, where $\rho_0^{(c)}$ and $\rho_\infty^{(c)}$ are the equilibrium bulk densities at coexistence. Finally, the components g_{ij} the metric tensor (see figure A1) are obtained by substituting equations (D.7) into (A.7). The metric tensor is required to compute the MLP, Γ. The kinetic coefficient $g(s)$,

equation (5), can be readily written in terms of the components g_{ij} when Γ is re-parameterized in terms of ρ_0 (i.e., $R = R_\Gamma(\rho_0)$) by using equation (A.18):

$$g[\Gamma] = g_{\rho_0,\rho_0}(\rho_0) + 2g_{\rho_0,R}(\rho_0)\frac{\mathrm{d}R}{d\rho_0} + g_{R,R}(\rho_0)\left(\frac{\mathrm{d}R}{d\rho_0}\right)^2, \tag{D.10}$$

with the metric components given as follows:

$$g_{R,R}(\rho_0) = \frac{4\pi}{5}\frac{(\rho_0-\rho_\infty)^2}{(\rho_\infty-\rho_0 y^3)}R^3\frac{1}{(1+y+y^2)^3} \times\left(\begin{array}{c}(5+6y+3y^2+y^3)+3y^2(1+3y+y^2)\dfrac{\mathrm{d}R_1}{\mathrm{d}R}\\ +y^3(1+3y+6y^2+5y^3)\left(\dfrac{\mathrm{d}R_1}{\mathrm{d}R}\right)^2\end{array}\right) \tag{D.11}$$

$$g_{R,\rho_0}(\rho_0) = \frac{4\pi}{30}\frac{(\rho_0-\rho_\infty)}{\rho_\infty-\rho_0 y^3}R^4\frac{1-y}{(1+y+y^2)^2} \times\left(\begin{array}{c}2(5+6y+3y^2+y^3)\\ +3y^2(1+3y+y^2)\dfrac{\mathrm{d}R_1}{\mathrm{d}R}\\ +3y(1+3y+y^2)\left(\dfrac{3}{R_1}\dfrac{(\rho_0-\rho_\infty)}{(1-y^3)}\dfrac{\mathrm{d}R_1}{\mathrm{d}\rho_0}\right)\\ +2y^2(1+3y+6y^2+5y^3)\dfrac{\mathrm{d}R_1}{\mathrm{d}R}\left(\dfrac{3}{R_1}\dfrac{(\rho_0-\rho_\infty)}{(1-y^3)}\dfrac{\mathrm{d}R_1}{\mathrm{d}\rho_0}\right)\end{array}\right) \tag{D.12}$$

$$g_{\rho_0,\rho_0}(\rho_0) = \frac{4\pi}{45}\frac{R^5}{\rho_0} + \frac{4\pi}{45}\frac{1}{(\rho_\infty-\rho_0 y^3)}R^5\frac{(1-y)^2}{1+y+y^2} \times\left(\begin{array}{c}(5+6y+3y^2+y^3)\\ +3y(1+3y+y^2)\left(\dfrac{3}{R_1}\dfrac{(\rho_0-\rho_\infty)}{(1-y^3)}\dfrac{\mathrm{d}R_1}{\mathrm{d}\rho_0}\right)\\ +y(1+3y+6y^2+5y^3)\left(\dfrac{3}{R_1}\dfrac{(\rho_0-\rho_\infty)}{(1-y^3)}\dfrac{\mathrm{d}R_1}{\mathrm{d}\rho_0}\right)^2\end{array}\right) \tag{D.13}$$

where we have introduced $y = R/R_1$ for simplicity.

ORCID iDs

Serafim Kalliadasis https://orcid.org/0000-0001-9858-3504

References

[1] Kashchiev D 2000 *Nucleation: Basic Theory with Applications* (Oxford: Butterworth-Heinemann)
[2] Kelton K and Greer A 2010 *Nucleation in Condensed Matter: Applications in Materials and Biology* (*Pergamon Materials Series*) (Amsterdam: Elsevier)
[3] Carstens J C 1979 Drop growth in the atmosphere by condensation: application to cloud physics *Adv. Colloid Interface Sci.* **10** 285–314
[4] Knight C A 1979 Ice nucleation in the atmosphere *Adv. Colloid Interface Sci.* **10** 369–95
[5] Michelangeli D V, Toon O B, Haberle R M and Pollack J B 1993 Numerical simulations of the formation and evolution of water ice clouds in the Martian atmosphere *Icarus* **102** 261–85
[6] Wang Y *et al* 2012 The predominant role of collagen in the nucleation, growth, structure and orientation of bone apatite *Nat. Mater.* **11** 724–33
[7] Veis A and Dorvee J R 2013 Biomineralization Mechanisms: a new paradigm for crystal nucleation in organic matricies *Calcified Tissue Int.* **93** 307–15
[8] Driessche A, Kellermeier M, Benning L G and Gebauer D 2016 *New Perspectives on Mineral Nucleation and Growth: From Solution Precursors to Solid Materials* (Berlin: Springer)
[9] Wetzel R 2006 Nucleation of huntingtin aggregation in cells *Nat. Chem. Biol.* **2** 297–8
[10] Koopmann R *et al* 2012 *In vivo* protein crystallization opens new routes in structural biology *Nat. Methods* **9** 259–62
[11] Duszenko M *et al* 2015 *In vivo* protein crystallization in combination with highly brilliant radiation sources offers novel opportunities for the structural analysis of post-translationally modified eukaryotic proteins *Acta Crystallogr.* F **71** 929–37
[12] Kapusta J I 1984 Nucleation rate for black holes *Phys. Rev.* D **30** 831–2
[13] Blander M 1979 Bubble nucleation in liquids *Adv. Colloid Interface Sci.* **10** 1–32
[14] Gibbs J W 1878 On the equilibrium of heterogeneous substances *Trans. Connecticut Acad.* **3** 343–524

[15] Gibbs J W 1878 On the equilibrium of heterogeneous substances *Trans. Connecticut Acad.* **3** 108–248
[16] Volmer M and Weber A 1926 Nuclei formation in supersaturated states (transl.) *Z. Phys. Chem.* **119** 277–301
[17] Volmer M 1939 Kinetik der Phasenbildung (*Chemische Reaktion*) (Dresden: Steinkopff)
[18] Farkas L 1927 The speed of germinitive formation in supersaturated vapours (transl.) *Z. Phys. Chem.* **125** 236–42
[19] Becker R and Döring W 1935 Kinetic treatment of grain-formation in super-saturated vapours *Ann. Phys.* **24** 719–52
[20] Frenkel I J 1946 *Kinetic Theory of Liquids* (Oxford: Oxford University Press)
[21] Zeldovich J B 1943 On the theory of new phase formation *Acta Physicochim. URSS* **18** 1–22
[22] Schöpe H J, Bryant G and van Megen W 2006 Two-step crystallization kinetics in colloidal hard-sphere systems *Phys. Rev. Lett.* **96** 175701
[23] Gliko O *et al* 2007 Metastable liquid clusters in super- and undersaturated protein solutions *J. Phys. Chem.* B **111** 3106–14
[24] Cöelfen H and Antonietti M 2008 *Mesocrystals and Nonclassical Crystallization* (New York: Wiley)
[25] Vekilov P G, Pan W, Gliko O, Katsonis P and Galkin O 2009 Metastable mesoscopic phases in concentrated protein solutions *Aspects of Physical Biology* (*Lecture Notes in Physics*) ed G Franzese and M Rubi 752 (Berlin: Springer) pp 65–95
[26] Vekilov P G 2010 Nucleation *Cryst. Growth Des.* **10** 5007–19
[27] Gebauer D and Cölfen H 2011 Prenucleation clusters and non-classical nucleation *Nano Today* **6** 564–84
[28] De Yoreo J 2013 Crystal nucleation: more than one pathway *Nat. Mater.* **12** 284–5
[29] Vekilov P G and Vorontsova M A 2014 Nucleation precursors in protein crystallization *Acta Crystallogr.* F **70** 271–82
[30] Tan P, Xu N and Xu L 2014 Visualizing kinetic pathways of homogeneous nucleation in colloidal crystallization *Nat. Phys.* **10** 73–9
[31] Sleutel M and Van Driessche A E S 2014 Role of clusters in nonclassical nucleation and growth of protein crystals *Proc. Natl Acad. Sci. USA* **111** E546–53
[32] Sauter A *et al* 2014 Nonclassical pathways of protein crystallization in the presence of multivalent metal ions *Cryst. Growth Des.* **14** 6357–66
[33] Lu Y, Lu X, Qin Z and Shen J 2015 Experimental evidence for ordered precursor foreshadowing crystal nucleation in colloidal system *Solid State Commun.* **217** 13–6
[34] Vorontsova M A, Chan H Y, Lubchenko V and Vekilov P G 2015 Lack of dependence of the sizes of the mesoscopic protein clusters on electrostatics *Biophys. J.* **109** 1959–68
[35] Bonn D and Shahidzadeh N 2016 Multistep crystallization processes: how not to make perfect single crystals *Proc. Natl Acad. Sci. USA* **113** 13551–3
[36] Russo J and Tanaka H 2016 Nonclassical pathways of crystallization in colloidal systems *MRS Bull.* **41** 369–74
[37] Lee S *et al* 2016 Multiple pathways of crystal nucleation in an extremely supersaturated aqueous potassium dihydrogen phosphate (KDP) solution droplet *Proc. Natl Acad. Sci. USA* **113** 13618–23
[38] Karthika S, Radhakrishnan T K and Kalaichelvi P 2016 A review of classical and nonclassical nucleation theories *Cryst. Growth Des.* **16** 6663–81
[39] Evans J S 2017 Polymorphs, proteins, and nucleation theory: a critical analysis *Minerals* **7** 62
[40] Wolde P R t and Frenkel D 1997 Enhancement of protein crystal nucleation by critical density fluctuations *Science* **277** 1975–8
[41] Qi W, Peng Y, Han Y, Bowles R K and Dijkstra M 2015 Nonclassical nucleation in a solid-solid transition of confined hard spheres *Phys. Rev. Lett.* **115** 185701
[42] Iwamatsu M 2012 Steady-state nucleation rate and flux of composite nucleus at saddle point *J. Chem. Phys.* **136** 204702
[43] Landau L D, Lifshitz E M and Pitaevskij L P 1980 *Statistical Physics: Part 2 : Theory of Condensed State* (Oxford: Pergamon)
[44] Durán-Olivencia M A, Yatsyshin P, Goddard B D and Kalliadasis S 2017 General framework for fluctuating dynamic density functional theory *New J. Phys.* **19** 123022
[45] Lutsko J F 2012 A dynamical theory of nucleation for colloids and macromolecules *J. Chem. Phys.* **136** 034509
[46] Lutsko J F and Durán-Olivencia M A 2013 Classical nucleation theory from a dynamical approach to nucleation *J. Chem. Phys* **138** 244908
[47] Lutsko J F and Durán-Olivencia M A 2015 A two-parameter extension of classical nucleation theory *J. Phys.: Condens. Matter* **27** 235101
[48] Durán-Olivencia M A and Lutsko J F 2015 Mesoscopic nucleation theory for confined systems: a one-parameter model *Phys. Rev.* E **91** 022402
[49] Sleutel M, Lutsko J, Van Driessche A E S, Durán-Olivencia M A and Maes D 2014 Observing classical nucleation theory at work by monitoring phase transitions with molecular precision *Nat. Commun.* **5** 5598
[50] Lutsko J F and Nicolis G 2006 Theoretical evidence for a dense fluid precursor to crystallization *Phys. Rev. Lett* **96** 046102
[51] Lutsko J 2010 Recent developments in classical density functional theory *Adv. Chem. Phys.* **144** 1–92
[52] Goddard B D, Nold A, Savva N, Pavliotis G A and Kalliadasis S 2012 General dynamical density functional theory for classical fluids *Phys. Rev. Lett.* **109** 120603
[53] Yatsyshin P, Parry A O, Rascón C and Kalliadasis S 2017 Classical density functional study of wetting transitions on nanopatterned surfaces *J. Phys.: Condens. Matter* **29** 094001
[54] Langer J S 1969 Statistical theory of the decay of metastable states *Ann. Phys.* **54** 258–75
[55] Langer J S and Turski L A 1973 Hydrodynamic model of the condensation of a vapor near its critical point *Phys. Rev.* A **8** 3230–43
[56] Hänggi P, Talkner P and Borkovec M 1990 Reaction-rate theory: fifty years after Kramers *Rev. Mod. Phys.* **62** 251–341
[57] Carnahan N F and Starling K E 1969 Equation of state for nonattracting rigid spheres *J. Chem. Phys.* **51** 635–6
[58] Hansen J and McDonald I 1986 *Theory of Simple Liquids* (San Diego, CA: Academic)
[59] Strey R, Wagner P E and Viisanen Y 1994 The problem of measuring homogeneous nucleation rates and the molecular contents of nuclei: progress in the form of nucleation pulse measurements *J. Phys. Chem.* **98** 7748–58
[60] Gharibeh M *et al* 2005 Homogeneous nucleation of n-propanol, n-butanol, and n-pentanol in a supersonic nozzle *J. Chem. Phys.* **122** 094512
[61] Ford I J 1997 Nucleation theorems, the statistical mechanics of molecular clusters, and a revision of classical nucleation theory *Phys. Rev.* E **56** 5615–29
[62] Risken H 1996 *The Fokker–Planck Equation: Methods of Solutions and Applications* 2nd edn (Berlin: Springer)
[63] Frenkel I J 1939 Statistical theory of condensation phenomena *J. Chem. Phys.* **7** 200–1